Elucidation of the redox activity of Ca2MnO3.5 and CaV2O4 in calcium batteries using operando XRD: charge compensation mechanism and reversibility

Ashley Black, Carlos Frontera, Arturo Torres, Miguel Recio-Poo, Patrick Rozier, Juan Forero-Saboya, François Fauth, Esteban Urones-Garrote, M. Elena Arroyo-de Dompablo, M. Rosa Palacín

Energy Storage Materials 47 (2022) 354–364

Contents lists available at ScienceDirect

Energy Storage Materials

journal homepage: www.elsevier.com/locate/ensm

Elucidation of the redox activity of $Ca_2MnO_{3.5}$ and CaV_2O_4 in calcium batteries using operando XRD: charge compensation mechanism and reversibility

Ashley P. Black[a], Carlos Frontera[a], Arturo Torres[b], Miguel Recio-Poo[b], Patrick Rozier[c], Juan D. Forero-Saboya[a], François Fauth[d], Esteban Urones-Garrote[e], M. Elena Arroyo-de Dompablo[b,*], M. Rosa Palacín[a,*]

[a] Institut de Ciència de Materials de Barcelona, ICMAB-CSIC, Campus UAB, 08193 Bellaterra, Catalonia, Spain
[b] Departamento de Química Inorgánica, Universidad Complutense de Madrid, Madrid 28040, Spain
[c] University of Toulouse III Paul Sabatier, CIRIMAT CNRS UMR 5085, 31062 Toulouse Cedex 09, France
[d] CELLS - ALBA synchrotron, 08290 Cerdanyola del Vallès, Catalonia, Spain
[e] Centro Nacional de Microscopía Electrónica (CNME), Universidad Complutense de Madrid, Madrid 28040, Spain

ARTICLE INFO

Keywords:
calcium batteries
positive electrode
calcium vanadium oxide
calcium manganese oxide
anion-deficient perovskites
DFT

ABSTRACT

$Ca_2MnO_{3.5}$ and CaV_2O_4 were found to be potentially interesting as positive electrode materials for calcium metal-based high-energy density batteries with DFT-predicted average voltages of 3.7 V and 2.5 V and energy barriers for Ca migration of 1.1 eV and 0.6 eV, respectively. Both compounds were prepared by solid state reaction under reducing atmospheres. Optimum conditions to achieve $Ca_2MnO_{3.5}$ comprised the reduction of Ca_2MnO_4 under NH_3 gas at 420^{0}C with a flow rate of 1200 ml/min while CaV_2O_4 was achieved by reduction of CaV_2O_6 at 700 ^{0}C under H_2 flow. Electrochemical oxidation of $Ca_2MnO_{3.5}$ in lithium or calcium cells resulted in the formation of an orthorhombic phase with cell parameter (a= 5.2891(1), b= 10.551(2), c= 12.1422(1)). *Operando* synchrotron radiation diffraction experiments indicate that the charge compensation mechanism is not related to Ca^{2+} extraction but to intercalation of F^- (originated from electrolyte salt decomposition) into the anion vacancy position, as confirmed by EELS and EDS. This process was found to be irreversible. In the case of CaV_2O_4, oxidation induces the electrochemical extraction of calcium with the formation of an orthorhombic phase (space group *Pbnm*) with cell parameters a = 10.72008(9) Å, b = 9.20213(2) Å and c = 2.89418(3) Å. The process was also investigated via *operando* synchrotron radiation diffraction, with the oxidized phase being found to reintercalate Ca^{2+} ions upon reduction, with the formation of a solid solution. Preliminary cycling tests reveals a decrease in the polarization after the first cycle and call for further investigation of this system.

1. Introduction

Li-ion batteries (LIB) have been continuously improving performance and reducing cost since its commercialization [1] and are currently expanding their field of application from electronics to transportation and even grid storage. Nonetheless, the technology is now reaching its fundamental limits in terms of energy density. The “holy grail” to leap-frog present values would be to develop rechargeable batteries using metals as negative electrodes. Besides the intensive research on concepts based on lithium metal such as Li-S and Li-air, recent efforts are targeting the exploration of divalent metals [2]. In contrast to lithium, Ca and Mg are both very abundant in the Earth’s crust, ranked 5th and 8th, respectively, with the raw materials being lower in price than the lithium counterparts. Their capacities, despite lower than lithium metal, are much higher than those of the graphite based negative electrodes typically employed in LIBs. Proof-of-concept of a Mg metal based battery was provided already in 2000 [3], but its commercialization has remained elusive due to the corrosive nature and low stability of the electrolytes employed and the fundamental limited diffusion of highly polarizing Mg^{2+} ions. Ca metal based batteries have been much less explored but recent proof-of-concept of electrolytes enabling successful plating and stripping of the metal catalyzed activity in the field [4]. Indeed, estimates of prospective figures of merit at the cell level using open energy-cost models [5] indicate that performances comparable to state-of-the art LIB could be achieved with positive electrodes exhibiting moderate potential (2.5V) and a capacity of 200 mAh/g, and that volu-

* Corresponding authors: M.E. Arroyo-de Dompablo, Departamento de Química Inorgánica, Universidad Complutense de Madrid, Madrid 28040, Spain, M.R. Palacin, ICMAB: Institut de Ciencia de Materials de Barcelona, Campus UAB, 08193 Bellaterra, Spain
E-mail addresses: e.arroyo@quim.ucm.es (M.E. Arroyo-de Dompablo), rosa.palacin@icmab.es (M.R. Palacín).

https://doi.org/10.1016/j.ensm.2022.02.017
Received 17 November 2021; Received in revised form 4 February 2022; Accepted 10 February 2022
Available online 12 February 2022

metric energy densities above 1000 Wh/l would be possible considering the same capacity but operation at 3V [6].

In spite of such nice expectations, the investigation of suitable positive electrode materials has been plagued with a number of hurdles. On one hand, the lack of standard electrolytes and protocols may result in side reactions inducing misinterpretation of the electrochemical response achieved [7–9], which makes real bulk activity difficult to elucidate unless complementary characterization techniques are used [10]. On the other, testing of materials similar to those used in the LIB field which would enable reversible intercalation/de-intercalation of calcium has to date led to the identification of few active compounds of limited performance (V_2O_5, TiS_2, MoO_3, Prussian blue analogs…). Besides those, some structural frameworks were identified which enable electrochemical de-intercalation of calcium, such as 1D Ca_3CoMO_6 (M=Co, Mn) [11], for which the process was found to be irreversible likely due to the structural changes taking place upon reduction resulting in too high migration barriers for calcium ions [12]. These findings highlight the complexity of achieving materials with reversible Ca^{2+} intercalation and acceptable performance.

In contrast, successful calcium intercalation into chemically or electrochemically oxidized polyanionic frameworks (e.g. $Na_{1.5-x}VPO_{4.8}F_{0.7}$, $Na_{3-y}V_2(PO_4)_3$ or $Li_{1-z}FePO_4$) has been recently reported [13–15], with the positions of calcium in the crystal structure being elucidated in the case of the vanadium containing materials. Yet, since these compounds do contain lithium or sodium, an additional treatment, either chemical or electrochemical, is required to remove these alternative ions, which is an extra hurdle for practical applications. Otherwise, the exploration of organic electrode materials, not involving an intercalation redox mechanism, seems also promising [16].

Within this scenario, a DFT driven research approach is clearly a powerful strategy to shortcut the meandrous that a classical trial and error method will encounter along its way. Several works [17–20] deal with the systematic search of potential positive electrodes for calcium batteries among large databases of compounds, such as the Inorganic crystal data base (ICSD), the Materials Project (MP) or the American Mineralogist Crystal Structure Database (AMCSD). From this compendium of computational results, it is concluded that the major obstacle for viable Ca-cathodes is the sluggish diffusion of Ca^{2+} ions in inorganic structures. Computationally, the ionic diffusivity (D) can be inferred from the calculated migration barrier energy (Em) [21]·. Canepa *et al.* explored the tolerable energy barrier for an optimum electrode performance as a function of the C-rate, temperature and particle size [20,22]. For a nanosized compound, an energy barrier below 0.65 eV is required to achieve a C/2 battery operation rate (here D ~ 10^{-12} cm^2 s^{-1}) at room temperature. The tolerable energy barrier can be increased by lowering the rate / particle size or increasing the temperature. For instance, the tolerable energy for 10 nm particles operating at 66 °C at a C/6 rate raises to 0.895 eV . Full details of the relationship between the migration barrier and the maximum particle size permitting reasonable diffusivity, at various variation C-rates and temperatures, are given by Lu *et al.* [20] and Canepa *et al.* [22]. These values of tolerable migration energies are useful indicators in the quest for positive electrode materials. Indeed, experiments evidence that compounds with predicted energy barriers for calcium diffusion above ~1 eV are inactive, even at very low C rates (C/100) and temperatures of ~ 50 °C. Examples of those materials are perovskite-$CaMoO_3$ (Em = 1.8 eV) [23], $CaMn_2O_4$ (Em= 1.3 eV) [24], CaV_2O_5 (Em=1.6-1.9) [25–27], brownmillerite-$Ca_2Fe_2O_5$ (Em=1 eV) [27,28], and $CaTaN_2$ (Em=1.7 eV) [8]. On the other hand, when energy barriers are lower than 1 eV, some electrochemical activity is often observed, examples being TiS_2 (Em= 0.75 eV) [10], $VOPO_4$ (Em= 0.5 eV) [19,29], $Ca_4Fe_9O_{17}$ (Em = 0.72 eV) [28] or $Ca_3Co_2O_6$ (Em= 0.9 eV) [12].

It should be noted that the previous DFT-quests for Ca-cathodes mostly focus in materials that, as discussed above, can be synthetized in the discharged (or reduced) state, this is to say, containing Ca ions in the structure. Following with this research line, in this work we will show that DFT calculations enabled the identification of CaV_2O_4 and $Ca_2MnO_{3.5}$ as potential positive electrodes for calcium batteries [30,31]. The experimental investigation confirmed the viability and reversibility of deintercalation for CaV_2O_4, while in the case of $Ca_2MnO_{3.5}$, an alternative charge compensation mechanism for manganese oxidation was encountered.

2. Materials and methods

a) Computational

Calculations have been performed using the *ab-initio* total-energy and molecular dynamics program VASP (Vienna Ab-initio Simulation Program) developed at the Universität Wien [32]. Total energy calculations based on Density Functional Theory (DFT) were performed within the Generalized Gradient Approximation (GGA), with the exchange and correlation functional form developed by Perdew, Burke, and Ernzerhof (PBE) [33]. The interaction of core electrons with the nuclei is described by the Projector Augmented Wave (PAW) method. The energy cut off for the plane wave basis set was kept fix at a constant value of 600 eV throughout the calculations. The integration in the Brillouin zone is done on appropriate k-point sets determined by the Monkhorst-Pack scheme. A convergence of the total energy close to 10 meV per formula unit is achieved with such parameters. Spin polarized calculations considering a ferromagnetic configuration were performed in all cases. All crystal structures were fully relaxed (atomic positions, cell parameters and volume). The final energies of the optimized geometries were recalculated so as to correct the changes in the basis set of wave functions during relaxation. To take electron correlation into account, the total energies of the GGA-optimized compounds have been calculated using the GGA+U method, with U_{eff} of 3 and 4 eV for the *d*- states of V and Mn, respectively [34].

The crystal models for the initial compounds were taken from the ICSD files 164185- CaV_2O_4[35] and 62168-$Ca_2MnO_{3.5}$[36]. The crystal models for the fully deintercalated phases were constructed removing all the Ca ions from the relaxed structures of the initial Ca-bearing compounds. To simulate the crystal structures of the possible partially deinserted compounds it is necessary to establish an ordered pattern of Ca ions and vacancies. Hence Ca-vacancy arrangements were created using the CASM (Cluster Approach to Statistical Mechanics) software package [37]. Search for pseudo symmetry in the final optimized models was done using the PLATON software [38].

The average Ca intercalation voltages have been obtained from the calculated total energies of the calciated and decalciated forms, following the methodology described by Aydinol et al. [39]. The Ca^{2+} mobility is investigated using the Nudged Elastic Band method (NEB) as implemented in VASP [40]. NEB calculations are usually carried out at the dilute limits, that is, either the migration of a single vacancy in an otherwise fully inserted structure or a single ion migration in an otherwise calcium-free host structure. To attain the dilute limit, we used a superstructure of the unit cell that guarantees a minimum interaction between defects. Constant volume calculations were performed within the GGA (and eventually GGA+U) approximation, considering a sufficient number of intermediate images initialized by linear interpolation between the two fully relaxed end points. To calculate the energy at the saddle point, cubic splines were fit through the images along each hop.

b) Experimental

Ca_2MnO_4 was synthesized following the Pechini method [41]. $Mn(NO_3)_2 \cdot 9H_2O$ (Aldrich 99%), $Ca(NO_3)_2 \cdot 4H_2O$ (Aldrich 99.95%), $C_6H_8O_7$ (citric acid, Aldrich 99.5%) and $C_2H_6O_2$ (ethylene glycol) were subsequently dissolved in water in a molar ratio of Ca: Mn: $C_6H_8O_7$: $C_2H_6O_2$ = 2: 1: 3: 1. The solution was kept under continuous stirring at 80°C until complete evaporation. The resulting citrate complexes were decomposed in air at 500°C for 6 h to yield an amorphous carbonate

mixture. Finally, polycrystalline Ca_2MnO_4 was obtained by calcination of the precursor at 1000°C for 24 h and used to achieve $Ca_2MnO_{3.5}$ under NH_3 flow (Carburos Metálicos 99.9%) after optimizing synthesis conditions (see Section 3b).

CaV_2O_4 was synthesized according to the method reported by Hastings *et al.* [42]. The CaV_2O_6 precursor was prepared by solid state reaction between $CaCO_3$ and V_2O_5 (650°C, 12 hours, air atmosphere) and treated under H_2 gas at 700°C for 4 hours to yield pure CaV_2O_4.

X-Ray powder diffraction patterns were acquired on a Bruker D8 Advance A25 diffractometer in a Debye-Scherrer configuration equipped with a Mo Kα1 radiation source (λ = 0.7093 Å) and Johansson monochromator. Synchrotron X-ray diffraction (SXRD) patterns where collected on the MSPD beamline [43] (ALBA synchrotron, Cerdanyola del Vallès, Spain) using the newly deployed position sensitive detector MYTHEN2 and λ=0.6200 Å. In both cases, the samples, either as prepared or recovered after running electrochemical experiments and dismantling cells inside an Ar filled glove box, were embedded in a 0.5 mm diameter borosilicate glass capillary and spun during data collection. *Operando* synchrotron diffraction experiments were carried out at the MSPD beamline using 5 mm diameter hole drilled 2032 coin cells equipped with a glass window and a setup enabling the alternative sequential measurement of eight cells in the same experiment [44]. Rietveld refinements and Fourier analysis were carried out with the Fullprof Suite program [45,46].

High-Angle Annular Dark-Field (HAADF) Scanning-Transmission Electron Microscopy (STEM) images were acquired with an ARM200 cF microscope, fitted with a corrector of the spherical aberration (resolution of 0.08 nm). Electron Energy-Loss spectroscopy (EELS) was performed in the same microscope, using a GIF Quantum ER spectrometer. The Mn-$L_{2,3}$ edges were acquired ($\beta\approx$30 mrad, acquisition time of 1 second, dispersion of 0.1 eV/pixel) in order to quantify the average oxidation state according to the white-lines ratio method [47] . The displacement of the absolute energy-loss value of the edge was compared between the different samples in order to check for the possible oxidation of Mn [48]. The average composition of the crystals was analyzed with X-Ray Energy Dispersive Spectroscopy (XEDS).

Tape casted electrodes were prepared from a mixture of as synthesized powder samples with carbon black (Super P, Timcal, Switzerland) and polyvinylidene difluoride (Arkema) in weight ratios of 80:10:10. A slurry was made by dispersing the active material, carbon and binder powders in N-methyl-2-pyrrolidone (Aldrich, ⩾99.9%) with a solid/solvent ratio of 100 mg/ml, which was then ball milled at 400 rpm for 1 h using a Retsch PM10 planetary mill, doctor blade casted (thickness 400 μm) on a 18 μm thick aluminum foil (Goodfellow, 99%) and vacuum dried at 120°C for 3 h. Electrode discs of 11 mm diameter with an average active material load of about 2 mg, were cut from the casted tape, pressed at 5 Tons and dried overnight in a vacuum chamber before use. Electrochemical tests were performed in three electrode Swagelok cells using activated carbon (AC, Kynol, ACC-509220) or Li metal as counter electrodes (CE) and an Ag wire was as reference electrode (RE), which was calibrated using a 10 mM ferrocene/ferrocenium solution in 0.45 $Ca(BF_4)_2$ in EC:PC following previously optimized protocols, its potential being 0.32 V vs NHE [49]. The electrolytes used were 0.45M $Ca(BF_4)_2$ dissolved in a 1:1 (v/v) mixture of ethylene carbonate (EC, Aldrich anhydrous 99.0%) and propylene carbonate (PC, Aldrich anhydrous 99.0%), prepared from $Ca(BF_4)_2 \cdot xH_2O$ salt (Alfa Aesar), 1M $LiPF_6$ in 1:1 (v/v) mixture of ethylene carbonate (EC) and dimethyl carbonate (DMC) (Solvionic, denoted LP30), 1M Lithium bis oxalato borate (LiBoB, Chemetal, Battery grade) or 0.45M cesium fluoride (CsF, Aldrich, 99%) in 1:1 (v/v) mixture of EC and PC. The water content in all electrolytes was measured by Karl Fisher titration and found to be lower than 50 ppm. Electrolyte preparation and cell assembling were done in an Ar filled glove box with less than 1 ppm of O_2 and H_2O. Prior to applying any current to the cells assembled, equilibration of the working electrode (WE) potential under the operating conditions at open circuit potential (OCP) was ensured. Tests were done using a Bio-Logic VMP3 potentiostat in galvanostatic mode with potential limitation (GCPL) at C/50 (equivalent to 1 mol of Ca^{+2} or 2 moles of e^- reacted in 50 h) at room temperature unless stated otherwise. *Operando diffraction* experiments were carried out at C/50 rate using the cells described in the previous sub-section containing 3 mg of powder electrode material prepared by mixing carbon black and the compound under study in weight ratios 25:75 and either activated carbon (AC) or Li metal as counter electrode and 0.45M $Ca(BF_4)_2$ in EC:PC or LP30 as electrolytes respectively.

3. Results and discussion

a) Computational

$Ca_2MnO_{3.5}$ is an oxygen-deficient compound derived from the first member of the Ruddlesden–Popper family $Ca_{n+1}Mn_nO_{3n+1}$, (Ca_2MnO_4, K_2NiF_4-type). The introduction of oxygen vacancies in the structure of Ca_2MnO_4 results in Mn^{3+} ions in square pyramidal coordination. Hence, the structure of $Ca_2MnO_{3.5}$ (space group *Bbcm*) consists of square pyramidal MnO_5 polyhedra linked by corners in the *ab* plane, forming rings of six MnO_5 units themselves sharing corners to form $[Mn_2O_7]$ layers (Figs. 1A-1C). Along the *c*-axis, in between two sheets of $[Mn_2O_7]$, there are two consecutive layers of calcium atoms which form a 8-fold coordination polyhedron, with Ca-O distances 2.3 Å x 2, 2.5 Å x 2, 2.6 Å x 2 and 3 Å x 2.

Fig. 1D shows the calculated energy barriers of Ca migration in a $2 \times 1 \times 1$ supercell of $Ca_2MnO_{3.5}$ ($Ca_{31}Mn_{16}O_{56}$ composition). Ca diffusion in the *ab* plane can involve different pathways, as shown in Fig. 1B. The calculated barriers of 1.1 and 1.2 eV in two different directions suggest that two-dimensional conductivity may take place. As discussed in the introduction, with in-plane energy barriers around 1 eV, $Ca_2MnO_{3.5}$ falls in the border-line between electrochemically active and inactive materials. As expected, Ca-diffusion along the *c*-axis of $Ca_2MnO_{3.5}$ is impeded as the calculated energy barriers are too high (above 1.8 eV, Fig. 1C). Regarding the electronic properties, the calculated DOS suggest a semiconducting behavior (see Figure S1).

Ca deinsertion from $Ca_2MnO_{3.5}$ is likely limited to the Mn^{3+}/Mn^{4+} redox couple (maximum specific capacity 140 mAh/g), according to the reaction:

$$Ca_2MnO_{3.5} \rightarrow 0.5\,Ca^{2+} + e^- + Ca_{1.5}MnO_{3.5} \quad (1)$$

For the $Ca_{1.5}MnO_{3.5}$ composition, vacancies and Ca^{2+} ions can adopt seven distinct arrangements within the primitive cell. The calculated average voltage taking the most stable configuration are 2.4 V (GGA) and 3.3 V (GGA+U). This would yield a maximum theoretical energy density of 462 mWh/g for this compound. Fig. 1E compares the crystal structure of the most stable configuration for $Ca_{1.5}MnO_{3.5}$ with that of the pristine material. A phase transformation is foreseen upon Ca-deintercalation, driven by the crystal field energies of Mn^{3+} and Mn^{4+} ions. Since Mn^{4+} has a d^3 electronic configuration, it has a strong tendency to adopt an octahedral coordination. This change in the Mn-polyhedra is achieved via the rearrangement of the square pyramids present in the *ab* plane of $Ca_2MnO_{3.5}$ (Fig. 1E left) so as to form double chains of square pyramids linked by corners to double chains of distorted octahedra in $Ca_{1.5}MnO_{3.5}$ (Fig. 1E right) . Note that the oxygen content is not compatible with a $Ca_{1.5}MnO_{3.5}$ structure consisting only of Mn-octahedra (K_2NiF_4 type). The phase transformation supposes a minimum volume contraction of 2% within both the GGA and GGA+U approximations (see Table S1 for lattice parameters).

CaV_2O_4 exhibits a crystal structure built up from edge-sharing chains of VO_6 octahedra, forming double rutile chains (Fig. 2A). Each double-rutile chain is connected to the adjacent chains through corner-sharing oxygen. As a result, tunnels appear in the framework along the *c* axis (space group *Pbnm*), where Ca ions occupy triangular prismatic sites with capped rectangular faces and Ca–O distances in the range 2.28–2.65 Å.

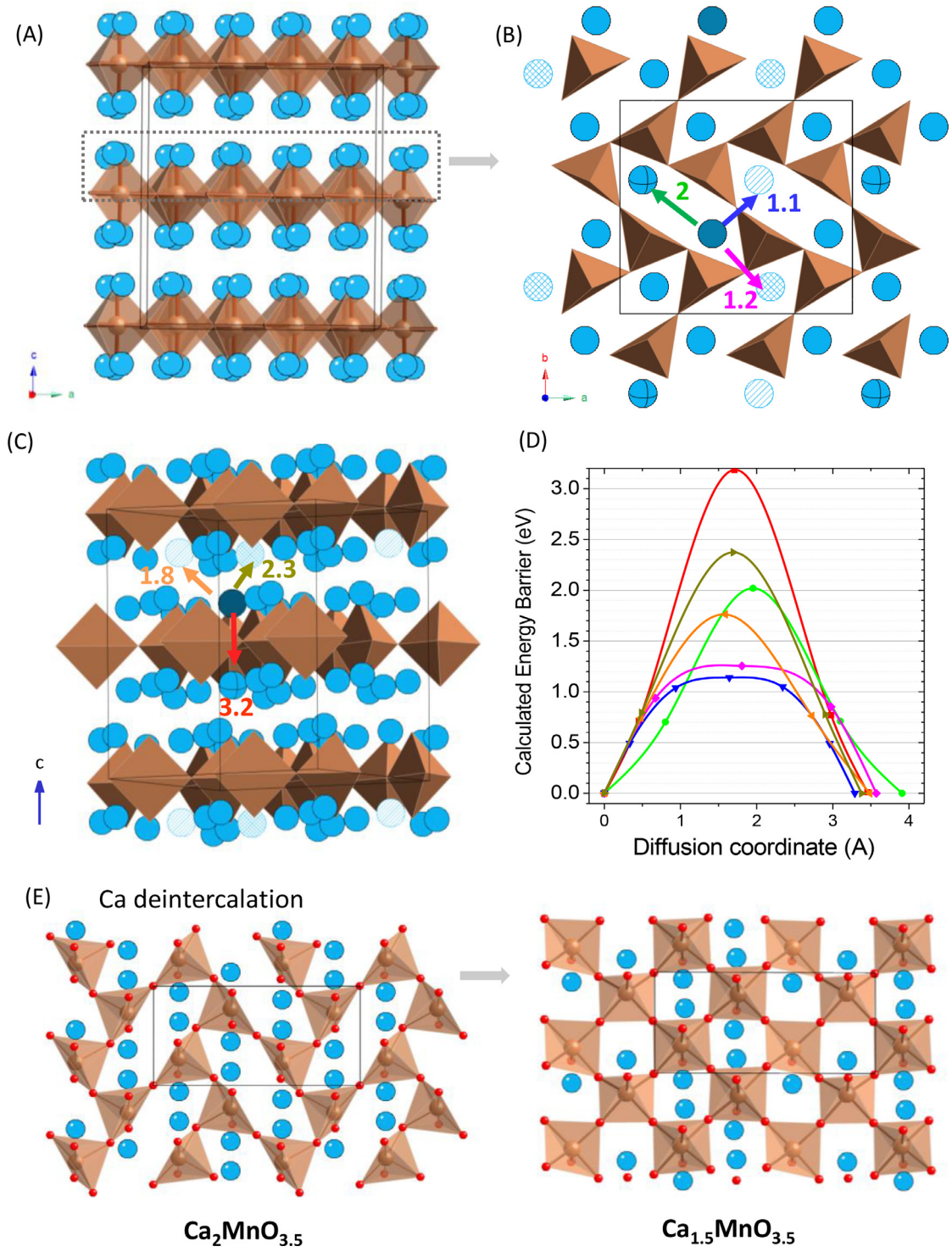

Fig. 1. Crystal structure of $Ca_2MnO_{3.5}$ (A). Investigated pathways for Ca diffusion in a 2 × 1 × 1 supercell. The initial Ca site is denoted by a dark-blue ball, and the final Ca sites by stripped balls. The numbers indicate the calculated energy migration barriers (in eV) (B,C). Calculated energy barriers for Ca diffusion in a $Ca_2MnO_{3.5}$ (D). View on the *ab* plane of the structures of the pristine material $Ca_2MnO_{3.5}$ and the deintercalated $Ca_{1.5}MnO_{3.5}$ (E). Color code: Ca blue, Mn brown, O red.

Topotactic calcium deintercalation (V^{3+}/V^{4+} redox couple) would result in a specific capacity of 260 mAh/g, following the reaction:

$$CaV_2O_4 \rightarrow Ca^{2+} + 2e^- + V_2O_4 \quad (2)$$

The calculated (GGA+U) cell lattice parameters for CaV_2O_4 (*a*= 10.791 *b* = 9.298 and *c* = 3.092) are in good agreement with experimental values, with errors below 2% (a = 10.6741(1) b = 9.2064 and c= 3.0090) [35] . The calculated lattice parameters of the hypothetical V_2O_4 are *a*= 10.355 Å *b*= 8.734 Å and *c* = 3.060 Å. Hence, according to DFT results, topotactic Ca deintercalation would cause the contraction of all lattice parameters, with a notorious unit cell volume reduction of 11% (from 310 $Å^3$ in CaV_2O_4 to 277 $Å^3$ in V_2O_4). The calcu-

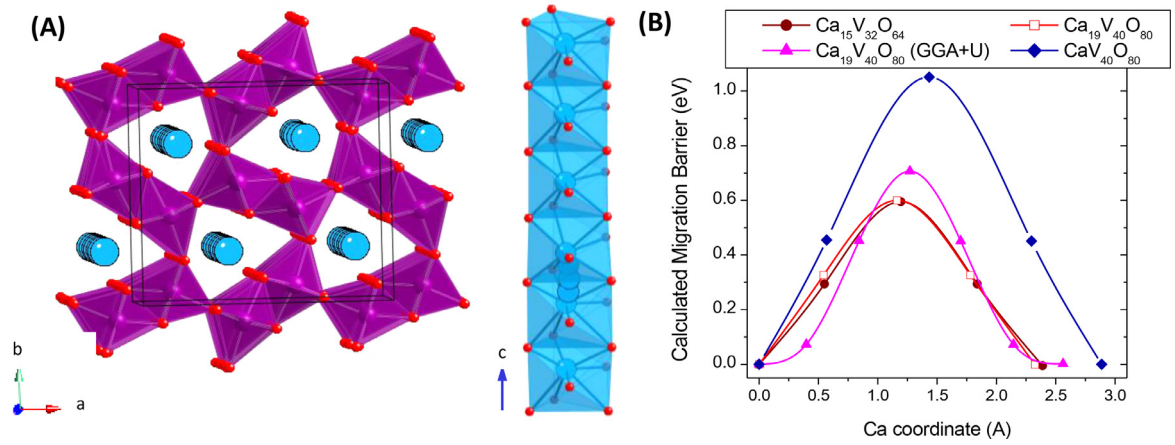

Fig. 2. Crystal structure of CaV_2O_4 and pathway for Ca diffusion (A). Calculated energy barriers for Ca diffusion in a $Ca_xV_2O_4$ (B). Color code: Ca blue, V purple, O red.

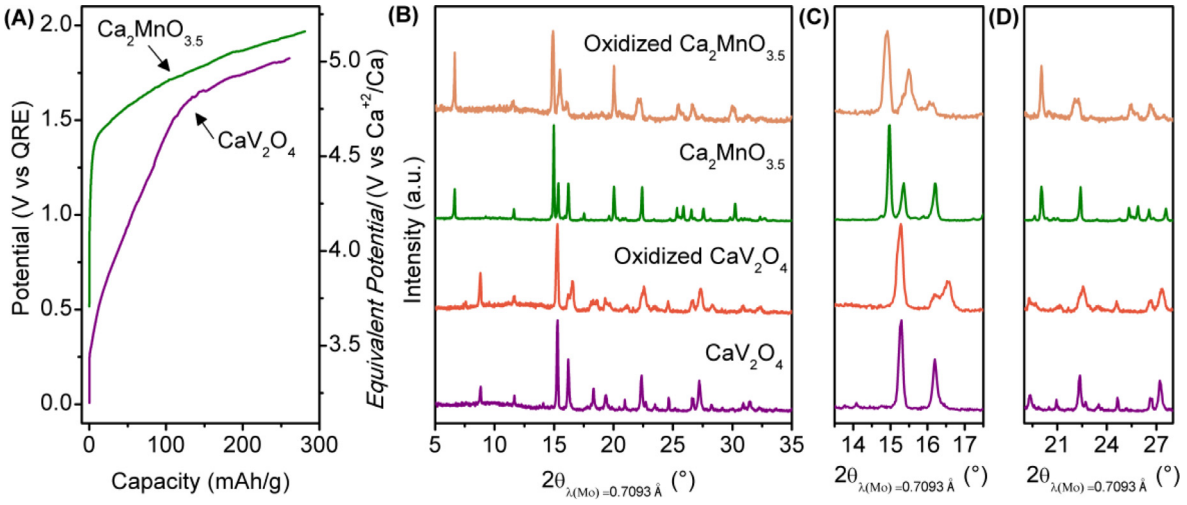

Fig. 3. Voltage vs capacity profiles for CaV_2O_4//AC cells (magenta curve) and $Ca_2MnO_{3.5}$//AC cells (green curve), using 0.45 M $Ca(BF_4)_2$ in EC:PC as electrolyte (A) and corresponding ex situ XRD patterns at the end of oxidation (B). The patterns corresponding to pristine CaV_2O_4 and $Ca_2MnO_{3.5}$ are also displayed for comparison. Expanded regions of the patterns are depicted in (C) and (D) so that the differences can be more clearly seen.

lated average deintercalation voltage (GGA+U) for reaction (2) is 2.48 V, in good agreement with previous DFT calculations [20]. This value results in an appealing theoretical energy density of 650 mWh/g for this compound.

The pathway for Ca^{2+} diffusion in CaV_2O_4 is along the tunnel built up by interconnected Ca sites (*c* axis in Fig. 2A). In this tunnel adjacent Ca sites share a triangular face and therefore on going from one site to the adjacent site the diffusing Ca ions must pass across this triangular window. The calculated energy barriers for Ca diffusion (Fig. 2B) are 0.60 eV (GGA) and 0.71 eV (GGA+U), similar to the value reported by Canepa´s group (GGA-Em of 0.654 eV) [20]. NEB calculations for the fully deintercalated phase (V_2O_4) yield a migration barrier of 1.05 eV (Fig. 2B), this is to say, too high to expect good Ca mobility. The energy barrier increase respective to CaV_2O_4 is related to the more constrained pathway for Ca diffusion in the lower volume cell of V_2O_4. Indeed, in the $CaFe_2O_4$-type compounds the GGA+U calculated migration barriers increase with the lower cell volume: CaV_2O_4 0. 71 eV, $CaFe_2O_4$ 0.75 eV, $CaCr_2O_4$ 0.87 eV and $CaCo_2O_4$ 1.03 eV (see Figure S2). In addition, enhanced electrostatic repulsions between the Ca ions and the more oxidized V^{+4} ions in V_2O_4 might play a role in the energy barrier increase.

b) Experimental

Synthesis

The synthesis of $Ca_2MnO_{3.5}$ by low temperature reduction of the Ruddlesden-Popper (n=1) Ca_2MnO_4 compound was reported by Poeppelmeier *et al.* [36,50] and found to require careful control of both the temperature and an appropriate reducing agent, with $Ca_2MnO_{3.5}$ being metastable and achievable only in a very narrow range of temperatures. The reduction of Ca_2MnO_4, synthesized as described above, was attempted at temperatures ranging between 300°C and 430°C with different reaction times under a variety of reducing atmospheres and gas flows. In 5% H_2/Ar atmosphere no evidence of the reduced $Ca_2MnO_{3.5}$ phase could be observed in the XRD pattern of the samples achieved after treatments at temperatures between 300°C and 350°C, and even after several 48h steps with intermediate regrinding Ca_2MnO_4 remained unreacted. At 380°C the characteristic reflections of the reduced phase started to appear with its amount being rather low even after consecutive regrinding and thermal treatment steps. Reaction of Ca_2MnO_4 at 400°C for 18h in 5% H_2/Ar led to the formation of a larger quantity of $Ca_2MnO_{3.5}$ together with a significant amount of the over reduced Mn^{2+}

containing the rock salt-type Ca_2MnO_3 phase. Analogous treatments were performed under 10% H_2/Ar leading to similar results. In light of such findings, the use of a less reducing atmosphere was deemed necessary and NH_3 was selected to that purpose. The strategy was successful, despite optimization of the protocol was required to minimize the amount of impurities (either Ca_2MnO_4 precursor and/or over reduced Ca_2MnO_3, both confirmed to be electrochemically inactive). Within the range of conditions systematically explored (see Figures S3-6 in S.I.) (temperature between 380 and 550°C, NH_3 flow between 50 and 1200 ml/min and time in the range from 4h to 50h), the best $Ca_2MnO_{3.5}$ batches obtained, and used for electrochemical characterization, contain less than 5% impurities (as deduced from Rietveld refinement) and were prepared by a short treatment (4h) under high ammonia flux (1200 ml/min) at 420°C.

Electrochemical characterization

In order to assess their electroactivity, attempts to extract Ca^{2+} from $Ca_2MnO_{3.5}$ and CaV_2O_4 were carried out in either Li or Ca cells at C rates ranging between 1C and C/100). Fig. 3A shows the characteristic voltage vs capacity profiles of $Ca_2MnO_{3.5}$ and CaV_2O_4 electrodes subjected to GCPL tests in three-electrode cells. Both exhibit an electrochemical response, with the potential being significantly higher for $Ca_2MnO_{3.5}$, in agreement with DFT results. The potential *vs*. capacity profile for the first oxidation of CaV_2O_4 follows a two-region trend, with a first steep sloping region from 0.25 V vs Ag QRE (equivalent to 3.5 V vs Ca^{+2}/Ca) up to 1.5 V and 130 mAh/g capacity and a second region extending to 260 mAh/g and 1.8 V vs Ag QRE. In contrast, for $Ca_2MnO_{3.5}$, the potential first increases rapidly to 1.4 V vs Ag QRE and then evolves gradually to reach 281 mAh/g at 1.9 V vs Ag QRE. The potential at the end of oxidation would be close to 5 V vs. Ca^{2+}/Ca in both cases and hence significant electrolyte oxidation can be expected to take place.

The *ex-situ* XRD data corresponding to the samples recovered after first oxidation to their nominal theoretical capacity are displayed in Fig. 3B. Patterns corresponding to oxidized CaV_2O_4 and $Ca_2MnO_{3.5}$ present significant changes when compared to those corresponding to the pristine compounds, which indicates that structural changes take place and would confirm the redox activity of these materials. In both cases, the formation of a new phase is observed upon oxidation with main reflections at 2θ (d) = 8.7° (4.62 Å), 15.25° (2.67 Å), 16.6°(2.46 Å), 22.5°(1.809 Å) and 27.2°(1.49 Å) and at 2θ = 6.7° (6.11 Å), 11.49° (2.73 Å), 14.89° (2.62 Å), 15.57° (2.04 Å) and 20.1° (1.85 Å) for CaV_2O_4 and $Ca_2MnO_{3.5}$respectively. A fraction of the pristine compound is still present in the XRD pattern collected after oxidation to the theoretical capacity value (considering Mn^{+4} and V^{+4} as the highest achievable oxidation states), in agreement with a certain contribution to the observed values of capacity resulting from electrolyte decomposition side reactions. These same new phases were also observed when electrochemical oxidation was performed in Li cells (LP30 electrolyte) for comparative purposes (see Figures S7 and S8 in the S.I.).

Operando *diffraction studies and charge compensation mechanism in* $Ca_2MnO_{3.5}$

The structural evolution of $Ca_2MnO_{3.5}$ electrodes was assessed by *operando* XRD using synchrotron radiation. Fig. 4A depicts the potential versus capacity profile and the corresponding XRD patterns. Oxidation of $Ca_2MnO_{3.5}$ was conducted for 40 h (equivalent to a capacity 220 mAh/g) before reversing the current upon reduction for the following 24h (equivalent to 140 mAh/g). The changes observed on the XRD patterns collected throughout the experiment highlight the progressive growth of peaks at $2\theta = 17.37^0$ and 18.15^0 upon oxidation to the expense of reflections at $2\theta = 17.50^0$, 17.96^0 and 18.96^0 (see Region I, Fig. 4A). Upon reduction, no changes in the patterns are evidenced, which point at the irreversibility of the redox process and therefore the capacity achieved being most likely related to side reactions involving the electrolyte. Further structural characterization of the new phase formed (denoted Ox-$Ca_2MnO_{3.5}$ from here on) was conducted by Rietveld refinement of the patterns obtained at the end of oxidation.

Fig. 4B represents the observed and calculated X-ray diffraction patterns of Ox-$Ca_2MnO_{3.5}$. Its crystal structure seems to be closely related to that of Ruddlesden-Popper Ca_2MnO_4, (space group *$I4_1/acd$*). (See Tables S2 to S5 for detailed structural and refinement parameters for Ca_2MnO_4 and $Ca_2MnO_{3.5}$). A first refinement of the Ox-$Ca_2MnO_{3.5}$ diffraction pattern performed in the tetragonal *$I4_1/acd$* space group resulted in cell parameter values of a = 5.2681(2) Å and c = 24.3730(16) Å and a cell volume of 676.41(6) Å^3 (V/Z= 84.553 Å^3), representing a volume expansion of nearly 4% with respect to Ca_2MnO_4 and $Ca_2MnO_{3.5}$ which have cell volumes of 650.28(3) Å^3 (V/Z= 81.283 Å^3) and 651.77(4) Å^3 (V/Z= 81.471 Å^3) respectively. Note that the volume difference between Ca_2MnO_4 and $Ca_2MnO_{3.5}$ can be ascribed to the larger volume of Mn^{+3} polyhedron (compared to that of Mn^{4+}), although it is partially compensated by lower oxygen content. In contrast, the volume expansion upon oxidation of $Ca_2MnO_{3.5}$ is contrary to what would be expected for Ca deinsertion concomitant to Mn^{3+} to Mn^{4+} oxidation, and also to DFT predictions. The refinement of the calcium content in Ox-$Ca_2MnO_{3.5}$ renders, within the error, no difference with respect to $Ca_2MnO_{3.5}$, which brings us to consider charge compensation mechanisms for manganese oxidation different from Ca extraction.

Due to the anion deficient nature of $Ca_2MnO_{3.5}$ and considering the evolution towards a crystal structure closely related to the Ca_2MnO_4 upon oxidation (consistent with the rearrangement predicted by DFT), anion intercalation appears as a reasonable alternative. This process might involve either large anions present in the electrolyte (BF_4^- or PF_6^-), which would likely induce larger structural changes, or other anions produced by their decomposition, such as F^- which would seem *a priori* more plausible. In order to further elucidate these aspects, $Ca_2MnO_{3.5}$ and Ox-$Ca_2MnO_{3.5}$ were characterized by HAADF-STEM, EDS and EELS. $Ca_2MnO_{3.5}$ consists of thick particles of 150-200 nm (see S.I.) and the HAADF-STEM images taken along the [-110] and [010] zone axis evidence a well crystallized sample (Fig. 5A). The characteristic lamellar structure of a Ruddlesden-Popper phase is identified with the intense bright spots corresponding to Mn atoms and the slightly less intense spots corresponding to the Ca atoms. The EDS measurements indicate a Ca:Mn atomic ratio consistent with the $Ca_2MnO_{3.5}$ formula. Upon oxidation, less order is observed (see Figure S10 in the S.I.). The Ca:Mn ratio of the pristine sample is preserved in most of the Ox-$Ca_2MnO_{3.5}$ crystallites; noteworthy, fluorine is clearly detected with approximate contents ranking from 6 to 12 % (see S.I. for EDS spectra). The EELS spectra depicted in Fig. 5B indicate a shift in the Mn-$L_{2,3}$ edge when comparing Ox-$Ca_2MnO_{3.5}$ and $Ca_2MnO_{3.5}$, which is consistent with Mn^{3+} oxidation during the electrochemical treatment. Nevertheless, the degree of Mn oxidation is inhomogeneous, in agreement with the variable F content detected in the Ox-$Ca_2MnO_{3.5}$ crystallites.

Attempting to confirm fluoride intercalation as the charge compensation mechanism upon oxidation, additional experiments were carried out involving the electrochemical oxidation of $Ca_2MnO_{3.5}$ in a fluorine free electrolyte (1M LiBoB in EC:PC). No changes in the diffraction pattern of the pristine material were detected even after prolonged oxidation. This suggests that Ca ions are not deintercalated from the crystal structure of $Ca_2MnO_{3.5}$, which is in agreement with the high DFT-migration barriers (> 1 eV). In contrast, electrochemical oxidation in an alternative F^- containing electrolyte (0.45M CsF in EC:PC) resulted in the observation of the peaks characteristic of Ox-$Ca_2MnO_{3.5}$, which confirms that the redox activity is related to fluoride intercalation in the crystal structure (see Figure S11). These findings are consistent with the known behavior of Ruddlesden-Popper type structures when tested as positive electrode materials in fluoride ion batteries (FIB) [51].

Taking into account the proposed insertion of fluoride ions in $Ca_2MnO_{3.5}$, the synchrotron XRD powder diffraction pattern of Ox-$Ca_2MnO_{3.5}$ was refined in the orthorhombic *Bbcm* space group and the

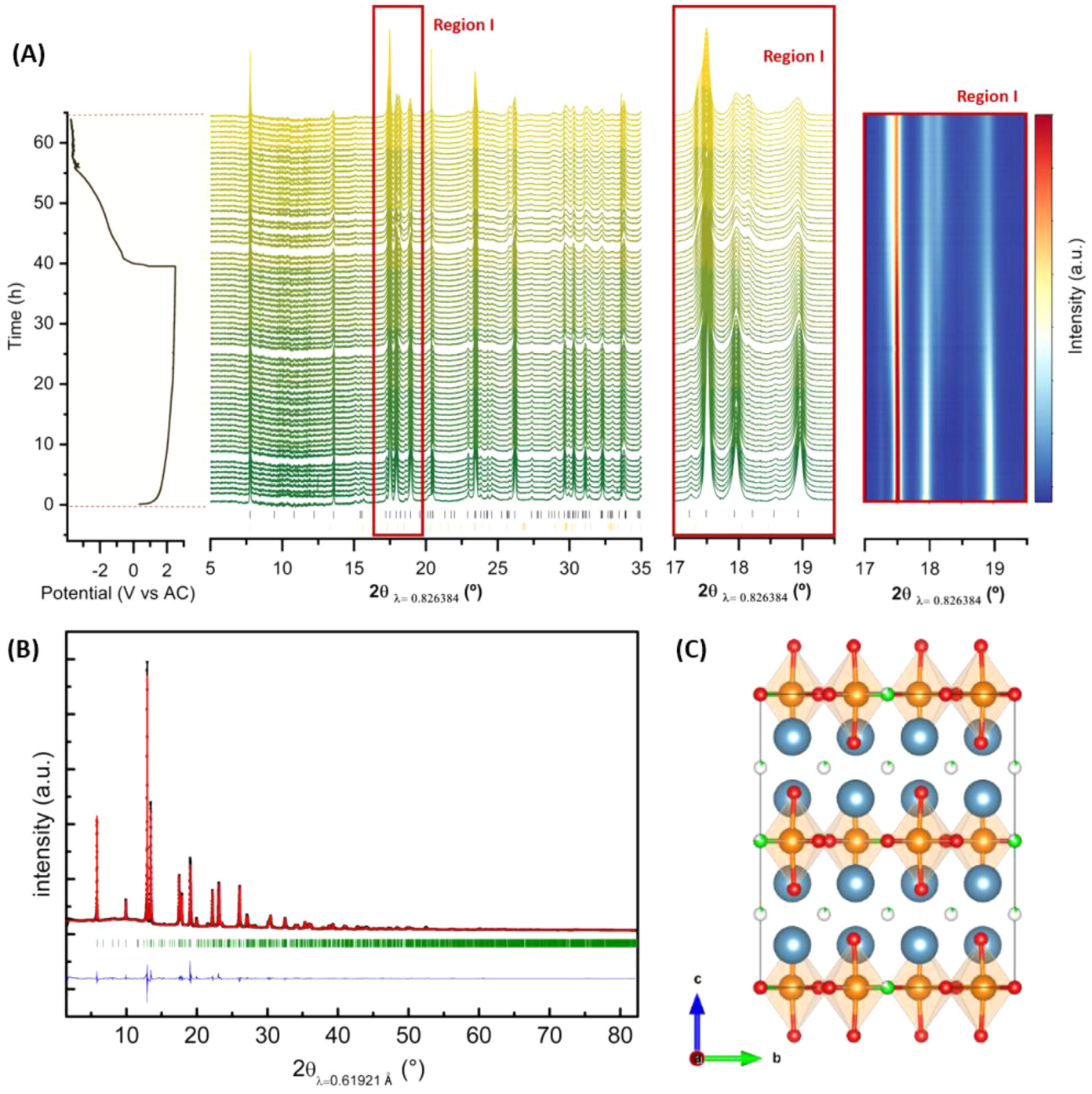

Fig. 4. Characteristic voltage versus time profile for a $Ca_2MnO_{3.5}$ // AC cell using 0.45M $Ca(BF_4)_2$ in EC:PC as electrolyte and corresponding *operando* synchrotron XRD patterns (A). Calculated and observed XRD patterns for $Ca_2MnO_{3.5}$ electrodes after oxidation in LP30 electrolyte (B). Structural model for $Ca_2MnO_{3.5}F_{0.6}$ (C) used for the calculated pattern.

difference Fourier map calculated in order to identify possible sites for fluorine (Figure S12). Fluorine occupancies were then refined in the crystallographic sites corresponding to the anion "vacancy" position (Wyckoff position 4b $\frac{1}{2}$,0,0). Fourier maps also show some significant missing electron density between CaO_2 planes, where some F^- insertion has been reported for Ruddlesden-Popper phases as well [51], as this position is suitable for the accommodation of additional anions [52]. The final refinement performed in the orthorhombic *Bbcm* space group resulted in cell parameter values of a = 5.2891(1) Å, b = 10.5509(2) Å and c = 12.1422(1) Å and a cell volume of 677.59(2) Å^3. It is worth mentioning that the electron density in 4*b* position of *Bbcm* space group is split, which could indicate that the true symmetry of the phase is lower or that some degree of F^- disorder exists, but no further reliable conclusions could be extracted from the available data. Refinement of F occupancies rendered a final stoichiometry $Ca_2MnO_{3.5}F_{0.6}$which would indicate a Mn oxidation state of about +3.6, consistent with the larger volume with respect to Ca_2MnO_4, and with fluoride ions being present not only in the initial vacant anionic sites but also between CaO_2 planes.

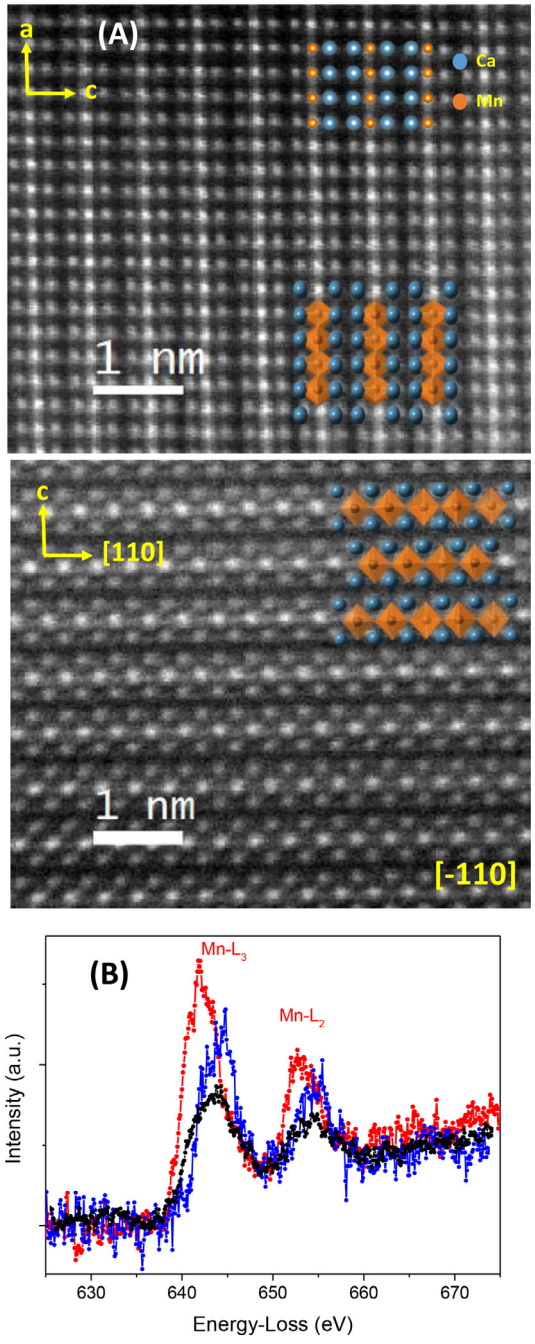

Fig. 5. Characteristic HAADF-STEM images of pristine $Ca_2MnO_{3.5}$(A). (EELS spectra of pristine $Ca_2MnO_{3.5}$ (in red), and oxidized crystallites with EDS deduced ratios of Ca:Mn:F of 58.0:31.4:10.6 (in blue) and 60.1:33.6:6.3 (in back). In the oxidized crystallites, the respective Mn oxidation states are +3.5 (blue spectra) and +3.3 (black spectra). Note that the formation of a Ruddlesden-Popper-like phase via fluoride insertion in $Ca_2MnO_{3.5}$ would yield the composition $Ca_2MnO_{3.5}F_{0.5}$, i.e. Ca:Mn:F ratio of 55.4: 38.0: 6.6 and Mn in a formal oxidation state of +3.5 (B)

Operando *diffraction studies and reversible Ca intercalation in* CaV_2O_4

The structural evolution of CaV_2O_4 upon electrochemical oxidation using 0.45 M $Ca(BF_4)_2$ in EC:PC as electrolyte was followed by *operando* synchrotron XRD. Fig. 6A shows the full patterns and expanded views of main diffraction peaks in regions I and II. Dark blue stripes in region II correspond to time in which diffraction data collection was unfortunately lost. The XRD patterns indicate gradual structural evolution of CaV_2O_4 upon oxidation and further reduction. In agreement with results achieved *ex situ*, new peaks appear at $2\theta = 13.26^0$ and 14.34^0 growing progressively upon oxidation to the expense of those at $2\theta = 13.34^0$ and 14.11^0, which gradually decrease in intensity indicating that a two-phase redox process takes place. Due to limited beamtime, the cell was switched to reduction without the oxidation being complete. The new peaks were seen to gradually shift to lower angles upon reduction, which would be consistent with the formation of a solid solution.

The refinement of a diffraction pattern of fully oxidized CaV_2O_4 achieved after a prolonged *ex-situ* oxidation is depicted in Fig. 6B and is consistent with no major structural changes taking place during oxidation and the space group being *Pbnm* as for the pristine compound. In contrast to what is observed for $Ca_2MnO_{3.5}$, the same phase is observed to form upon oxidation with all electrolyte compositions tested (with $Ca(BF_4)_2$, $LiPF_6$ or LiBoB as salts), which points at the charge compensation mechanism not involving fluoride ions for the case of CaV_2O_4. The refined values of the cell parameters for the oxidized phase are a = 10.72008(9) Å, b = 9.20213(2) Å and c = 2.89418(3) Å and the cell volume is 285.504(5) $Å^3$. This represents an expansion of 0.05 Å of the a lattice parameter, a c lattice parameter contraction = 0.09 Å and a volume contraction of 2.73 % respect to the pristine CaV_2O_4. This value is lower than the 11% contraction estimated by DFT for full oxidation of vanadium and removal of all calcium ions, but the lattice parameter variations are consistent with the extraction of calcium from the crystal structure (see Fig. 6C). The contraction of c likely results from the shrinking of VO_6 octahedra due to oxidation of vanadium. The expansion of the a lattice parameter is attributable to an increase of electrostatic repulsion between the anions as the shielding effect of Ca^{+2} ions decreases upon calcium extraction. The refinement of calcium occupancies in the oxidized phase renders a calcium content of 0.69 mol, indicating that ca. 0.3 mols of Ca^{+2} have been extracted from the crystal structure of CaV_2O_4. This value is consistent with the smaller contraction of the unit cell observed experimentally with respect to the DFT calculated value for V_2O_4. Fig. 6D depicts the fraction of pristine CaV_2O_4 and oxidized $Ca_xV_2O_4$ obtained by sequential refinement of *operando* XRD data (see some examples in the SI, Figure S13). The amount of $Ca_xV_2O_4$ is found to gradually increase upon oxidation to the expense of CaV_2O_4. Fig. 6E depicts the evolution of the total Ca:V_2O_4 ratio and the value of x in the $Ca_xV_2O_4$ oxidized phase, except for the initial patterns where its fraction is too low to obtain a reliable occupancy of Ca. Upon oxidation, a gradual decrease in the total amount of calcium is observed, while no changes are detected in x, in agreement with a two phase process taking place. Despite the current being switched upon reduction at t=32h, changes in the trend of the patterns are not clearly visible until a few hours later, which is likely due to sluggish reaction kinetics, as denoted by the significant cell polarization. Upon reduction, no significant changes in the relative amounts of $Ca_xV_2O_4$ and CaV_2O_4 can be detected. Within the sloping region above -1V a slow and gradual increase in the value of x is observed, which further continues when the low voltage plateau is reached (t=47h), at a faster pace, with the shift of the (021)-(211) doublet at 14.42° to lower angles being clearly visible. The cell expansion associated to this shift occurs without any apparent diminution of peak intensity, in full agreement with a solid solution mechanism taking place in this region instead of a two-phase mechanism to fully revert to the pristine phase. Overall these findings would suggest a different mechanism upon oxidation (two-phase) and reduction (single phase). While it cannot be excluded that the energy barrier to reform the pristine structure is too high, the behavior may be different depending on the current applied if kinetic factors play a role.

Electrochemical testing of CaV_2O_4

The reversibility of the redox processes prompted us to carry out further electrochemical cycling tests on CaV_2O_4 (Fig. 7) in three electrode cells. To avoid excessive electrolyte degradation, capacity was limited

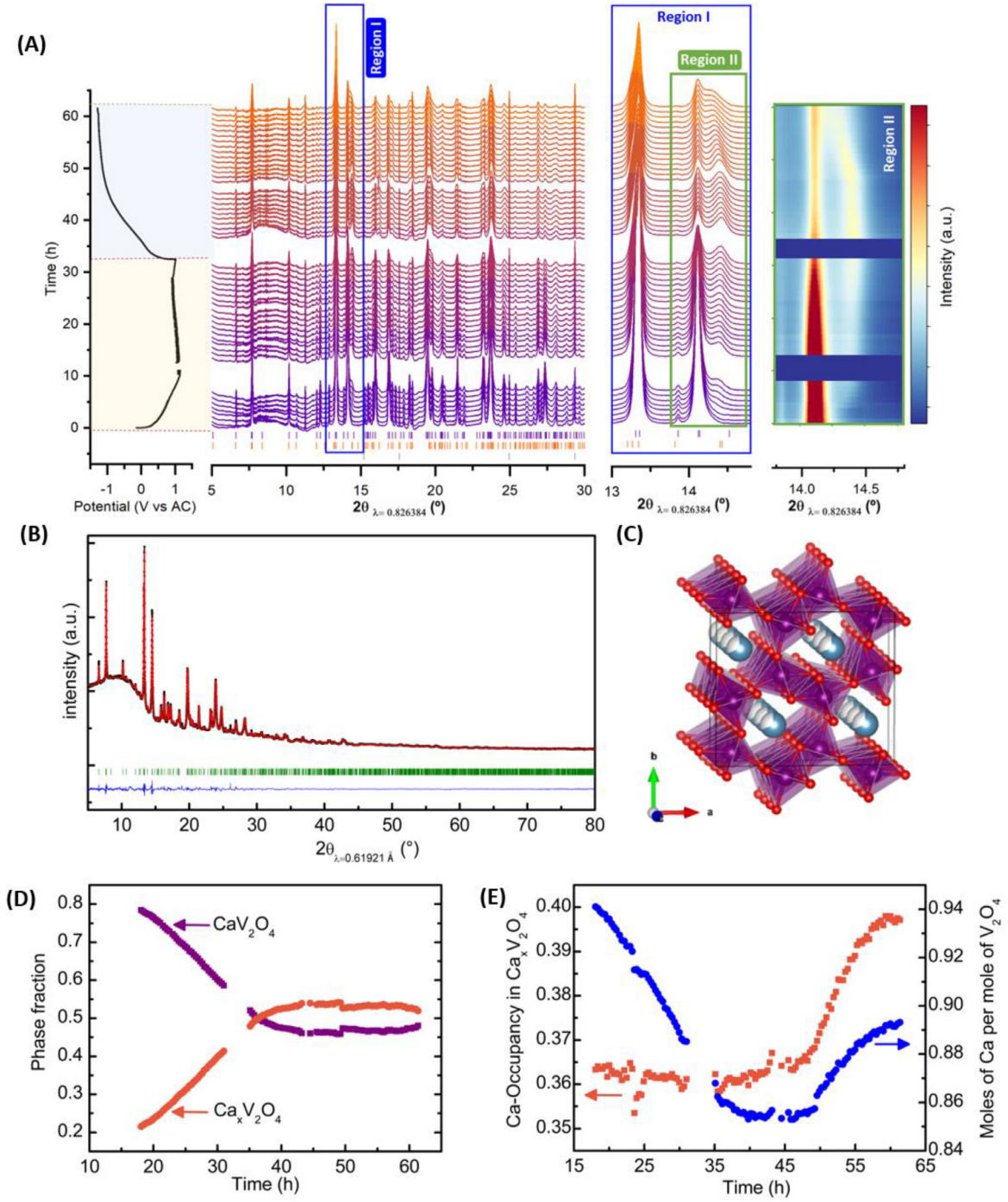

Fig. 6. Characteristic voltage versus time profile for a CaV_2O_4 // AC cell using 0.45M $Ca(BF_4)_2$ in EC:PC as electrolyte, and corresponding *operando* synchrotron XRD patterns (A). Calculated and observed patterns for CaV_2O_4 electrodes after full oxidation *ex-situ* in LP30 electrolyte (B). Structural model ofor $Ca_{0.7}V_2O_4$ (C). Phase fraction (D), calcium occupancies (note that x in $Ca_xV_2O_4$ equals $2Ca_{Occ}$), and the total amount of Ca (considering the two coexisting phases) (E) versus time obtained by sequential Rietveld refinement of *operando* XRD patterns.

between x=0 and x=0.25 in $Ca_{1-x}V_2O_4$ (65 mAh/g). Interestingly, the potential *vs* capacity profiles depict a significant decrease in the polarization after the first cycle, as the second oxidation starts at a potential ca. 500 mV lower than that of the first oxidation. For subsequent cycles the oxidation profile exhibits three distinct regions, with the length of the second plateau increasing upon cycling. It can be speculated that this could be related to enhanced active material utilization or to different reaction pathways (*i.e.* solid solution *vs*. two phase), but further experiments are needed to confirm these hypotheses. The reduction profile involves mainly a gradual decrease of the potential followed by a plateau at ca. -0.5 V vs Ag QRE. Experiments involving a longer oxidation step (between x=0 and x=0.60 (155mAh/g)), carried out at 50°C to enhance kinetics, yielded significantly larger capacities while keeping rather similar electrochemical responses. The most relevant difference between the profiles depicted in Fig. 7A and B is the clearer observation of diversesteps upon reduction for the latter, likely as a result of the oxidation proceeding to a larger extent. Overall, these preliminary experiments indicate that the redox mechanism deserves further investigation, including tests at different rates and temperatures, possibly involving also further *operando* studies.

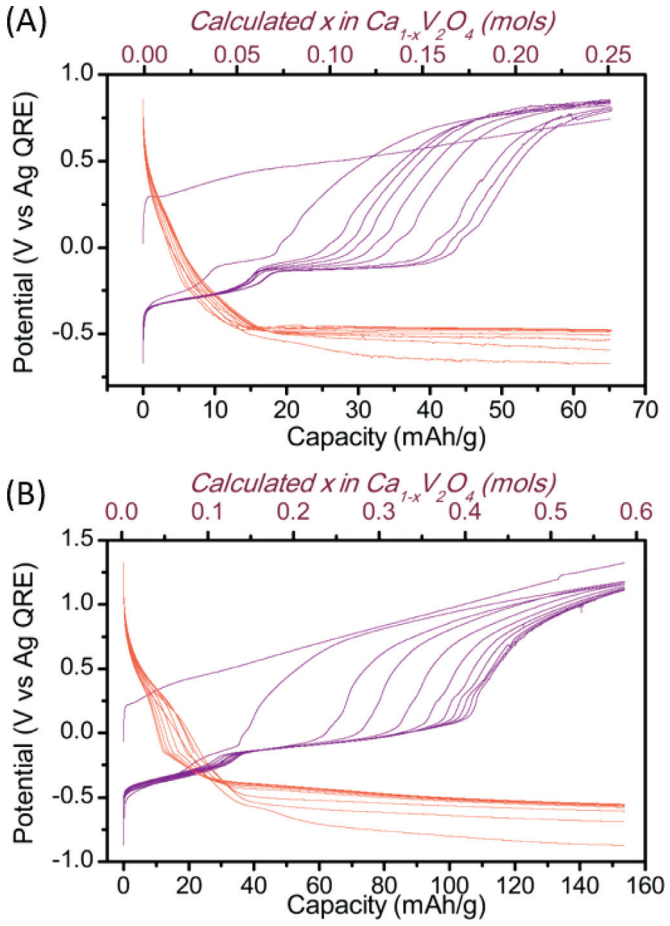

Fig. 7. Characteristic capacity vs. potential profiles for CaV_2O_4 // AC cells using 0.45M $Ca(BF_4)_2$ in EC:PC as electrolyte tested with capacity limitation at room temperature (***A***) and at 50°C (***B***), respectively. The capacity values are also expressed as calculated x in $Ca_xV_2O_4$ (top axis), considering that these are exclusively related to calcium extraction from the crystal structure. Oxidation and reduction steps are denoted in magenta and red respectively.

4. Conclusion

DFT calculations have enabled to identify $Ca_2MnO_{3.5}$ and CaV_2O_4 as potential positive electrode materials for calcium cells, and also provided some clues to sketch possible redox mechanisms. After synthesis of such compounds and complementary to electrochemical measurements, *operando* XRD has been critical to probe the charge compensation mechanism and reversibility of the redox reactions taking place.

$Ca_2MnO_{3.5}$ is an oxygen deficient compound (Mn is five-fold coordination) obtained by reduction of the Ruddlesden-Popper phase Ca_2MnO_4 (Mn in octahedral sites), which has been shown to oxidize in calcium cells, concomitant to a change in the crystal structure and the oxidation of manganese, as detected by EELS. *Operando* experiments enable to follow the oxidation process, which involves the formation of a new phase with no changes in the calcium stoichiometry. Fourier difference maps enable to detect the presence of additional fluoride ions in the crystal structure, which are generated through electrolyte decomposition of the electrolyte salt. The charge compensation mechanism for manganese oxidation is thus found to involve fluoride intercalation and not calcium extraction. This is fully consistent with DFT results disclosing the trend of Mn^{3+} polyhedra in $Ca_2MnO_{3.5}$ to regain the octahedral coordination upon Ca deintercalation and also with the high calculated energy diffusion barriers for calcium (above 1 eV).

In contrast, CaV_2O_4 exhibits an appealing energy barrier for Ca diffusion (~ 0.6 eV) which notoriously increases upon calcium extraction to yield virtual-V_2O_4 (~ 1 eV). Experimentally, the extraction of 0.3 moles of calcium upon oxidation was demonstrated by *operando* diffraction studies, with the formation of a new isostructural phase which upon reduction is found to re-intercalate calcium via a solid solution process. While further studies are needed to fully elucidate the redox mechanism, the results presented herein confirm the viability of reversibly extracting and reintercalating calcium ions in the crystal structure and call for further investigation of CaV_2O_4 as positive electrode material in calcium cells.

Declaration of Competing Interest

None.

CRediT authorship contribution statement

Ashley P. Black: Investigation, Formal analysis, Visualization, Writing – original draft. **Carlos Frontera:** Investigation, Formal analysis, Software, Visualization, Writing – review & editing. **Arturo Torres:** Investigation, Formal analysis, Visualization, Methodology, Writing – review & editing. **Miguel Recio-Poo:** Investigation, Formal analysis, Visualization, Writing – review & editing. **Patrick Rozier:** Investigation, Writing – review & editing. **Juan D. Forero-Saboya:** Investigation, Writing – review & editing. **François Fauth:** Investigation, Writing – review & editing. **Esteban Urones-Garrote:** Investigation, Formal analysis, Writing – review & editing, Visualization. **M. Elena Arroyo-de Dompablo:** Methodology, Conceptualization, Supervision, Project administration, Writing – original draft. **M. Rosa Palacín:** Conceptualization, Supervision, Project administration, Writing – original draft.

Acknowledgements

This research was funded by the European Union's Horizon 2020 research and innovation programme H2020 FETOPEN-1- 2016-2017 (CARBAT, grant agreement no. 766617). The authors are grateful for access to the computational facilities from Universidad de Oviedo (MALTA-Consolider cluster) and to ALBA synchrotron for beamtime (proposal 2021024935). ICMAB-CSIC members thank the Spanish Agencia Estatal de Investigación Severo Ochoa Programme for Centres of Excellence in R&D (CEX2019-000917-S).

Supplementary materials

Supplementary material associated with this article can be found, in the online version, at doi:10.1016/j.ensm.2022.02.017.

References

[1] T. Placke, R. Kloepsch, S. Dühnen, M. Winter, Lithium Ion, Lithium Metal, and Alternative Rechargeable Battery Technologies: The Odyssey for High Energy Density, Journal of Solid State Electrochemistry 21 (7) (2017), doi:10.1007/s10008-017-3610-7.
[2] A. Ponrouch, J. Bitenc, R. Dominko, N. Lindahl, P. Johansson, M.R. Palacin, Multivalent Rechargeable Batteries, Energy Storage Materials 20 (2019), doi:10.1016/j.ensm.2019.04.012.
[3] D. Aurbach, Z. Lu, A. Schechter, Y. Gofer, H. Gizbar, R. Turgeman, Y. Cohen, M. Moshkovich, E. Levi, Prototype Systems for Rechargeable Magnesium Batteries, Nature 407 (6805) (2000), doi:10.1038/35037553.
[4] M.E. Arroyo-de Dompablo, A. Ponrouch, P. Johansson, M.R. Palacín, Achievements, Challenges, and Prospects of Calcium Batteries, Chemical Reviews 120 (14) (2020), doi:10.1021/acs.chemrev.9b00339.
[5] E.J. Berg, C. Villevieille, D. Streich, S. Trabesinger, P. Novák, Rechargeable Batteries: Grasping for the Limits of Chemistry, Journal of The Electrochemical Society 162 (14) (2015), doi:10.1149/2.0081514jes.
[6] Monti, D.; Ponrouch, A.; Araujo, R. B.; Barde, F.; Johansson, P.; Palacín, M. R. Multivalent Batteries—Prospects for High Energy Density: Ca Batteries. *Frontiers in Chemistry*2019, 7. https://doi.org/10.3389/fchem.2019.00079.
[7] A.L. Lipson, D.L. Proffit, B. Pan, T.T. Fister, C. Liao, A.K. Burrell, J.T. Vaughey, B.J. Ingram, Current Collector Corrosion in Ca-Ion Batteries, Journal of The Electrochemical Society 162 (8) (2015), doi:10.1149/2.0811508jes.
[8] R. Verrelli, A.P. Black, C. Frontera, J. Oró-Solé, M.E. Arroyo-de Dompablo, A. Fuertes, M.R. Palacín, On the Study of Ca and Mg Deintercalation from Ternary Tantalum Nitrides, ACS Omega 4 (5) (2019), doi:10.1021/acsomega.9b00770.

[9] R. Dugas, J.D. Forero-Saboya, A. Ponrouch, Methods and Protocols for Reliable Electrochemical Testing in Post-Li Batteries (Na, K, Mg, and Ca), Chemistry of Materials 31 (21) (2019), doi:10.1021/acs.chemmater.9b02776.

[10] D.S. Tchitchekova, A. Ponrouch, R. Verrelli, T. Broux, C. Frontera, A. Sorrentino, F. Bardé, N. Biskup, M.E. Arroyo-de Dompablo, M.R. Palacín, Electrochemical Intercalation of Calcium and Magnesium in TiS_2: Fundamental Studies Related to Multivalent Battery Applications, Chemistry of Materials 30 (3) (2018), doi:10.1021/acs.chemmater.7b04406.

[11] A.P. Black, D. Monti, C. Frontera, D.S. Tchitchekova, R.G. Houdeville, F. Fauth, M.R. Palacin, *Operando* Synchrotron X-Ray Diffraction in Calcium Batteries: Insights into the Redox Activity of 1D Ca_3CoMO_6 (M = Co and Mn), Energy & Fuels 35 (13) (2021), doi:10.1021/acs.energyfuels.1c01343.

[12] A. Torres, F. Bardé, M.E. Arroyo-de Dompablo, Evaluation of Cobalt Oxides for Calcium Battery Cathode Applications, Solid State Ionics 340 (2019), doi:10.1016/j.ssi.2019.115004.

[13] B. Jeon, J.W. Heo, J. Hyoung, H.H. Kwak, D.M. Lee, S.-T. Hong, Reversible Calcium-Ion Insertion in NASICON-Type $NaV_2(PO_4)_3$, Chemistry of Materials 32 (20) (2020), doi:10.1021/acs.chemmater.0c01112.

[14] S. Kim, L. Yin, M.H. Lee, P. Parajuli, L. Blanc, T.T. Fister, H. Park, B.J. Kwon, B.J. Ingram, P. Zapol, R.F. Klie, K. Kang, L.F. Nazar, S.H. Lapidus, J.T. Vaughey, High-Voltage Phosphate Cathodes for Rechargeable Ca-Ion Batteries, ACS Energy Letters 5 (10) (2020), doi:10.1021/acsenergylett.0c01663.

[15] Z.-L. Xu, J. Park, J. Wang, H. Moon, G. Yoon, J. Lim, Y.-J. Ko, S.-P. Cho, S.-Y. Lee, K. Kang, A New High-Voltage Calcium Intercalation Host for Ultra-Stable and High-Power Calcium Rechargeable Batteries, Nature Communications 12 (1) (2021), doi:10.1038/s41467-021-23703-x.

[16] J. Bitenc, A. Scafuri, K. Pirnat, M. Lozinšek, I. Jerman, J. Grdadolnik, B. Fraisse, R. Berthelot, L. Stievano, R. Dominko, Electrochemical Performance and Mechanism of Calcium Metal-Organic Battery, Batteries & Supercaps 4 (1) (2021), doi:10.1002/batt.202000197.

[17] Z. Zhang, X. Zhang, X. Zhao, S. Yao, A. Chen, Z. Zhou, Computational Screening of Layered Materials for Multivalent Ion Batteries, ACS Omega 4 (4) (2019), doi:10.1021/acsomega.9b00482.

[18] A. Torres, F.J. Luque, J. Tortajada, M.E. Arroyo-de Dompablo, Analysis of Minerals as Electrode Materials for Ca-Based Rechargeable Batteries, Scientific Reports 9 (1) (2019), doi:10.1038/s41598-019-46002-4.

[19] A. Torres, J.L. Casals, M.E. Arroyo-de Dompablo, Enlisting Potential Cathode Materials for Rechargeable Ca Batteries, Chemistry of Materials 33 (7) (2021), doi:10.1021/acs.chemmater.0c04741.

[20] W. Lu, J. Wang, G. Sai Gautam, P. Canepa, Searching Ternary Oxides and Chalcogenides as Positive Electrodes for Calcium Batteries, Chemistry of Materials 33 (14) (2021), doi:10.1021/acs.chemmater.1c01992.

[21] D. Morgan, A. van der Ven, G. Ceder, Li Conductivity in Li_xMPO_4 (M = Mn, Fe, Co, Ni) Olivine Materials, Electrochemical and Solid-State Letters 7 (2) (2004), doi:10.1149/1.1633511.

[22] P. Canepa, G. Sai Gautam, D.C. Hannah, R. Malik, M. Liu, K.G. Gallagher, K.A. Persson, G. Ceder, Odyssey of Multivalent Cathode Materials: Open Questions and Future Challenges, Chemical Reviews 117 (5) (2017), doi:10.1021/acs.chemrev.6b00614.

[23] M.E. Arroyo-de Dompablo, C. Krich, J. Nava-Avendaño, M.R. Palacín, F. Bardé, In Quest of Cathode Materials for Ca Ion Batteries: The $CaMO_3$ Perovskites (M = Mo, Cr, Mn, Fe, Co, and Ni), Physical Chemistry Chemical Physics 18 (29) (2016), doi:10.1039/C6CP03381D.

[24] M.E.A. Dompablo, C. Krich, J. Nava-Avendaño, N. Biškup, M.R. Palacín, F. Bardé, A Joint Computational and Experimental Evaluation of $CaMn_2O_4$ Polymorphs as Cathode Materials for Ca Ion Batteries, Chemistry of Materials 28 (19) (2016), doi:10.1021/acs.chemmater.6b02146.

[25] R. Verrelli, A.P. Black, C. Pattanathummasid, D.S. Tchitchekova, A. Ponrouch, J. Oró-Solé, C. Frontera, F. Bardé, P. Rozier, M.R. Palacín, On the Strange Case of Divalent Ions Intercalation in V_2O_5, Journal of Power Sources 407 (2018), doi:10.1016/j.jpowsour.2018.08.024.

[26] G.S. Gautam, P. Canepa, R. Malik, M. Liu, K. Persson, G. Ceder, First-Principles Evaluation of Multi-Valent Cation Insertion into Orthorhombic V_2O_5, Chemical Communications 51 (71) (2015), doi:10.1039/C5CC04947D.

[27] A. Torres, F.J. Luque, J. Tortajada, M.E. Arroyo-de Dompablo, DFT Investigation of Ca Mobility in Reduced-Perovskite and Oxidized-Marokite Oxides, Energy Storage Materials 21 (2019), doi:10.1016/j.ensm.2019.06.002.

[28] A.P. Black, A. Torres, C. Frontera, M.R. Palacín, M.E. Arroyo-de Dompablo, Appraisal of Calcium Ferrites as Cathodes for Calcium Rechargeable Batteries: DFT, Synthesis, Characterization and Electrochemistry of $Ca_4Fe_9O_{17}$, Dalton Transactions 49 (8) (2020), doi:10.1039/C9DT04688G.

[29] J. Wang, S. Tan, F. Xiong, R. Yu, P. Wu, L. Cui, An, Q. $VOPO_4 \bullet 2H_2O$ as a New Cathode Material for Rechargeable Ca-Ion Batteries, Chemical Communications 56 (26) (2020), doi:10.1039/D0CC00772B.

[30] A.P. Black, M.R. Palacin, M.E. Arroyo-deDompablo, Electrode for Calcium Batteries and Its Manufacturing Method. EP21382186, March 5, 2021.

[31] A.P. Black, M.R. Palacin, M.E. Arroyo-deDompablo, Electrode of a Mixed Oxide for Calcium Batteries and Its Manufacturing Method. EP21382187, March 5, 2021.

[32] G. Kresse, J. Furthmüller, Efficient Iterative Schemes for *Ab Initio* Total-Energy Calculations Using a Plane-Wave Basis Set, Physical Review B 54 (16) (1996), doi:10.1103/PhysRevB.54.11169.

[33] J.P. Perdew, K. Burke, M. Ernzerhof, Generalized Gradient Approximation Made Simple, Physical Review Letters 77 (18) (1996), doi:10.1103/PhysRevLett.77.3865.

[34] A. Jain, S.P. Ong, G. Hautier, W. Chen, W.D. Richards, S. Dacek, S. Cholia, D. Gunter, D. Skinner, G. Ceder, K.A. Persson, Commentary: The Materials Project: A Materials Genome Approach to Accelerating Materials Innovation, APL Materials 1 (1) (2013), doi:10.1063/1.4812323.

[35] A. Niazi, S.L. Bud'ko, D.L. Schlagel, J.Q. Yan, T.A. Lograsso, A. Kreyssig, S. Das, S. Nandi, A.I. Goldman, A. Honecker, R.W. McCallum, M. Reehuis, O. Pieper, B. Lake, D.C. Johnston, Single-Crystal Growth, Crystallography, Magnetic Susceptibility, Heat Capacity, and Thermal Expansion of the Antiferromagnetic S=1 Chain Compound CaV_2O_4, Physical Review B 79 (10) (2009), doi:10.1103/PhysRevB.79.104432.

[36] M.E. Leonowicz, K.R. Poeppelmeier, J.M. Longo, Structure Determination of Ca_2MnO_4 and $Ca_2MnO_{3.5}$ by X-Ray and Neutron Methods, Journal of Solid State Chemistry 59 (1) (1985), doi:10.1016/0022-4596(85)90352-4.

[37] A. van der Ven, J.C. Thomas, Q. Xu, J. Bhattacharya, Linking the Electronic Structure of Solids to Their Thermodynamic and Kinetic Properties, Mathematics and Computers in Simulation 80 (7) (2010), doi:10.1016/j.matcom.2009.08.008.

[38] A.L. Spek, Structure Validation in Chemical Crystallography, Acta Crystallographica Section D Biological Crystallography 65 (2) (2009), doi:10.1107/S090744490804362X.

[39] M.K. Aydinol, A.F. Kohan, G. Ceder, K. Cho, J. Joannopoulos, *Ab Initio* Study of Lithium Intercalation in Metal Oxides and Metal Dichalcogenides, Physical Review B 56 (3) (1997), doi:10.1103/PhysRevB.56.1354.

[40] G. Mills, H. Jónsson, G.K. Schenter, Reversible Work Transition State Theory: Application to Dissociative Adsorption of Hydrogen, Surface Science 324 (2–3) (1995), doi:10.1016/0039-6028(94)00731-4.

[41] I.D. Fawcett, M. Sunstrom; Greenblatt, M. Croft, K.v. Ramanujachary, Structure, Magnetism, and Properties of Ruddlesden−Popper Calcium Manganates Prepared from Citrate Gels, Chemistry of Materials 10 (11) (1998), doi:10.1021/cm980380b.

[42] J.M. Hastings, L.M. Corliss, W. Kunnmann, S. la Placa, Magnetic Structure of Calcium Vanadite, Journal of Physics and Chemistry of Solids 28 (7) (1967), doi:10.1016/0022-3697(67)90051-0.

[43] F. Fauth, I. Peral, C. Popescu, M. Knapp, The New Material Science Powder Diffraction Beamline at ALBA Synchrotron, Powder Diffraction 28 (S2) (2013), doi:10.1017/S0885715613000900.

[44] M. Herklotz, J. Weiß, E. Ahrens, M. Yavuz, L. Mereacre, N. Kiziltas-Yavuz, C. Dräger, H. Ehrenberg, J. Eckert, F. Fauth, L. Giebeler, M. Knapp, A Novel High-Throughput Setup for *in Situ* Powder Diffraction on Coin Cell Batteries, Journal of Applied Crystallography 49 (1) (2016), doi:10.1107/S1600576715022165.

[45] J. Rodríguez-Carvajal, Recent Developments of the Program FULLPROF, Commission on Powder Diffraction (IUCr),Newsletter 26 (2001) 12–19.

[46] J. Rodríguez-Carvajal, Recent Advances in Magnetic Structure Determination by Neutron Powder Diffraction, Physica B: Condensed Matter 192 (1–2) (1993), doi:10.1016/0921-4526(93)90108-I.

[47] H.K. Schmid, W. Mader, Oxidation States of Mn and Fe in Various Compound Oxide Systems, Micron 37 (5) (2006), doi:10.1016/j.micron.2005.12.004.

[48] R.F. Egerton, Electron Energy-Loss Spectroscopy in the Electron Microscope, Springer US, Boston, MA, 2011, doi:10.1007/978-1-4419-9583-4.

[49] R. Verrelli, A. Black, R. Dugas, D. Tchitchekova, A. Ponrouch, M.R. Palacin, Steps Towards the Use of TiS_2 Electrodes in Ca Batteries, Journal of The Electrochemical Society 167 (7) (2020), doi:10.1149/1945-7111/ab7a82.

[50] K.R. Poeppelmeier, M.E. Leonowicz, J.M. Longo, $CaMnO_{2.5}$ and $Ca_2MnO_{3.5}$: New Oxygen-Defect Perovskite-Type Oxides, Journal of Solid State Chemistry 44 (1) (1982), doi:10.1016/0022-4596(82)90404-2.

[51] M.A. Nowroozi, I. Mohammad, P. Molaiyan, K. Wissel, A.R. Munnangi, O. Clemens, Fluoride Ion Batteries – Past, Present, and Future, Journal of Materials Chemistry A 9 (10) (2021), doi:10.1039/D0TA11656D.

[52] L.D. Aikens, R.K. Li, C. Greaves, The Synthesis and Structure of a New Oxide Fluoride, $LaSrMnO_4F$, with Staged Fluorine Insertion, Chemical Communications (21) (2000), doi:10.1039/b007045i.